Enhanced Ferroelectric and Visible-Light Photoelectric Properties in Multiferroic $KBiFe_2O_5$ via Pressure-Induced Phase Transition

Ganghua Zhang, Fengliang Liu, Tingting Gu, Yongsheng Zhao, Nana Li, Wenge Yang, and Shouhua Feng**

Ferroelectric (FE) photovoltaics have been drawing enormous attentions due to their superior potential.[1–3] Compared to traditional semiconductor solar cells, the bulk photovoltaic effect (BPVE) in FE relies on a polarization-induced internal electric field instead of p–n or Schottky junctions, which benefits the separation and migration of light-generated electron–hole pairs and reduces the cost of cell fabrication.[4–6] In order to cover the broader range of light absorption, many efforts have been focused on searching for narrow bandgap FE materials, such as $BiFeO_3$[2,5] and KBNNO.[7] However, the photocurrents obtained in these materials are still very low due to their high resistances and low carrier concentrations. In fact, a lot of strategies have been focused on improving the conductivity of the ferroelectrics to enhance their optoelectronic properties, e.g., the photoelectric properties of polycrystalline $BiFeO_3$ thin films can be improved by using graphene as top electrodes;[8] the highest light-conversion efficiencies among the ferroelectric photovoltaics have been achieved by incorporating more conductive Ag_2O (η = 0.195%)[9] and Cu_2O (η = 0.57%)[10] nanoparticles within ferroelectric $Pb(Zr_{1-x}Ti_x)O_3$ (PZT) films; increasing the tips of atomic force microscopy can enhance the photocurrent density and external quantum efficiency (EQE) by several orders of magnitude for $BiFeO_3$ single crystals.[11] Nevertheless, the uniformity of these composite materials is hard to control and the fabrication is commonly complex and costly, which may reduce the stability of the photovoltaic performance. More interestingly, several noncentrosymmetric FE-related compounds with metallic or semiconducting behavior, such as $LiOsO_3$,[12,13] $PbNiO_3$,[14] and $ZnPbO_3$,[15] have been discovered recently as a new class of materials with unconventional properties, providing an exotic playground for theorists and experimentalists in the photovoltaic field. As demonstrated in recent theoretical works,[16,17] "shift current" is the dominant mechanism for generating the BPVE in the ferroelectrics and a photocurrent in response to unpolarized light can be generated only in materials with nonzero polarization. Large shift current effects can be expected in materials with elemental combinations conducive to covalent bonding and delocalized electronic states. Thus, new polar materials with better ferroelectric and photoelectric performances are of great interest.

As a significant technique to modify the physical/chemical properties in current material science,[18–21] hydrostatic pressure has been considered as an efficient route to tune the crystal structure and electronic configuration for the photoelectric-related materials. Actually, the electrical conductivity of Nb-doped TiO_2[22] nanoparticles and Ta_2O_5[23] nanowires can be enhanced by pressure-induced phase transitions; the optical and electronic properties of GaAs nanowires can be improved by applying an external pressure;[24] the pressure-induced structure evolution and anomalous visible-light response have been studied in organometal halide perovskites;[25,26] the pressure-induced bandgap evolution and the Mott–Hubbard insulator–metal transition have been observed in multiferroic $BiFeO_3$.[27] Considering the excellent stability and controllability, hydrostatic pressure can not only offer an insight into the intrinsic relationship between crystal structure and its physical property, but also has immense potential of practical applications in photovoltaic devices as switcher or controller.

Up to now, there is no report about pressure effects on the photoelectric properties of FE materials, in spite of considerable modifications of the bandgaps and conductivity of many functional materials could be realized by the applied pressures. Among the room temperature FE materials, the newly synthesized single-crystal $KBiFe_2O_5$[28] possesses a suitable bandgap (1.6 eV) near the optimal bandgap (1.50 eV) for solar energy applications,[29] large light absorption coefficient $>10^4$ cm^{-1}

Dr. G. Zhang, Dr. F. Liu, Dr. T. Gu, Dr. Y. Zhao,
Dr. N. Li, Prof. W. Yang
Center for High Pressure Science and Technology
Advanced Research (HPSTAR)
Shanghai 201203, P. R. China
E-mail: yangwg@hpstar.ac.cn

Dr. F. Liu
Department of Physics
Fudan University
Shanghai 200433, P. R. China

Dr. Y. Zhao
State Key Laboratory of Superhard Materials
Jilin University
Changchun 130012, P. R. China

Prof. W. Yang
High Pressure Synergetic Consortium (HPSynC)
Geophysical Laboratory
Carnegie Institution of Washington
Argonne, IL 60439, USA

Prof. S. Feng
State Key Laboratory of Inorganic Synthesis and Preparative Chemistry
College of Chemistry
Jilin University
Changchun 130012, P. R. China
E-mail: shfeng@jlu.edu.cn

DOI: 10.1002/aelm.201600498

(comparable to CdTe[30] and CIGS solar cells[31]) and much lower bulk resistivity ≈10^7 Ω cm ($BiFeO_3$ ≈ 10^{10} Ω cm at ambient pressure as a comparison[32]). In this work, hydrostatic pressure up to 35 GPa has been applied to tune the crystal structure, bandgap, and ferroelectric and optoelectronic properties of the multiferroic $KBiFe_2O_5$. The pressure-induced crystal structure evolutions, ferroelectricity, and the visible-light photoresponse of $KBiFe_2O_5$ were studied by in situ X-ray diffraction (XRD), Raman spectrum, photoluminescence (PL) spectroscopy, electrical resistance, and optoelectronic and ferroelectric properties measurements. Enhanced electron transport, ferroelectric polarization, and visible light response have been achieved by pressure-induced phase transition, which suggest that the hydrostatic pressure techniques have great potential as versatile tools to tune the structural, ferroelectric and optoelectronic properties of the FE materials toward better photovoltaic performances.

The structure and morphology of as-grown crystalline $KBiFe_2O_5$ were characterized by XRD, scanning electron microscopy (SEM), and energy-dispersive spectrometer (EDS) (Figure S1, Supporting Information). The powder XRD data at room temperature can be indexed to orthorhombic space group $P2_1\,cn$ with cell parameters a = 7.988(2) Å, b = 11.819 (2) Å, c = 5.734(1) Å, which is identical to the calculated one using single-crystal data reported previously.[28] SEM photograph shows clearly that the morphology of the sample is rod-like small crystallites, ≈100–150 µm in a narrow particle-size distribution. EDX analysis of selected regions showed the presence of all four elements in the area analyzed with a constant ratio, which proofs the crystals with uniform chemical composition.

For in situ high-pressure structure study, the sample was loaded in a symmetrical diamond anvil cell (DAC) with neon as a pressure transmitting medium (see the Experimental Section). Synchrotron powder XRD patterns of $KBiFe_2O_5$ were collected at different pressures during compression up to 35 GPa and decompression. **Figure 1**a shows the 2D raw XRD patterns at several selected pressures, while Figure 1b shows all integrated 1D profiles. With increasing pressure, the sharp diffraction rings become weaker and broader. At 6.8 GPa, the appearance of several additional peaks suggests the onsite of phase transition. When the applied pressure exceeds 10.3 GPa, several diffraction peaks at 4.3° (200), 5.9° (131), 7.8° (150), and 8.7° (331) disappear and the broadening rings are transformed into sharp rings again, which can be associated with the completeness of phase transition. Under decompression to 0.4 GPa, the XRD profile is similar with the initial one, indicating a reversible phase transition. The HP phase was stable up to 35 GPa in this study. Upon decompression, the HP phase returns to the original low-pressure (LP) structure form confirmed by the analogous XRD patterns. This reversible pressure-induced structure evolution can be also confirmed by

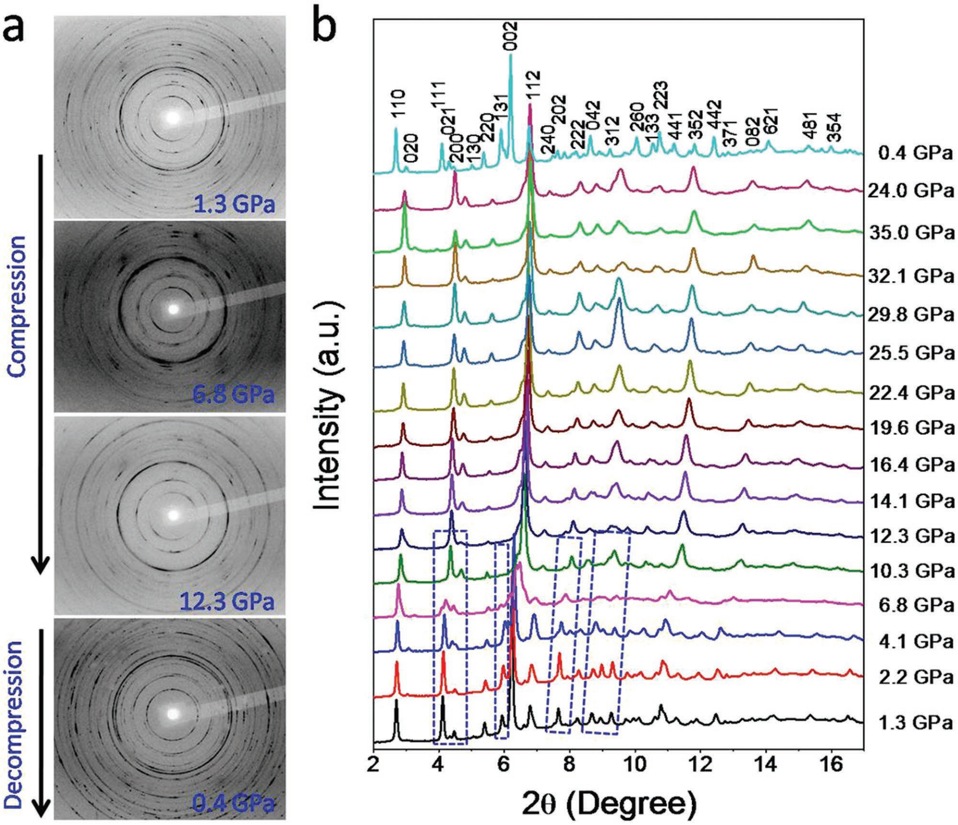

Figure 1. Selected synchrotron XRD patterns of $KBiFe_2O_5$ taken during compression up to 35.0 GPa and decompression. a) The raw 2D XRD patterns and b) integrated XRD 1D profiles. The rectangular boxes with dashed lines are for eye guide to highlight the diffraction peak shifting with applied pressure. The XRD pattern after decompression can be indexed with the same crystal structure (space group $P2_1\,cn$) of the pristine materials.

Raman spectroscopy collected during compression and decompression at room temperature (Figure S2, Supporting Information). From the Raman measurements, this phase transition starts at 5.9 GPa and completes at 9.2 GPa, which is close to the XRD results.

At ambient conditions, $KBiFe_2O_5$ presents a layered structure consisting of alternating blocks of $[Fe_2O_3]$ and $[(K,Bi)O_2]$ loosely connected by sharing some corner O atoms between the FeO_4 tetrahedra and BiO_6 octahedra (shown as inset in **Figure 2**a). In order to detect the pressure-induced local structure evolution, the Rietveld refinements were carried out on all XRD data. Under low pressure (<6 GPa), the integrated 1D XRD profiles can be well characterized by the orthorhombic $P2_1\,cn$ structure (see Figure 2a for the structure refinement). Above 10.3 GPa, a different orthorhombic symmetry with possible space group $Cmc2_1$ or *Ama*2 can be used to index the diffraction peaks based on the extinction rule. Both orthorhombic phases are noncentrosymmetric, suggesting the polarized feature of this HP phase of $KBiFe_2O_5$. Considering the slight atomic displacements and the symmetric relation compared to the initial structure model of $P2_1\,cn$, space group $Cmc2_1$ is more favorable than *Ama*2. Moreover, the Rietveld refinement with *Ama*2 symmetry gives a worse fitting intensity match (Figure S3, Supporting Information) than that with $Cmc2_1$ fitting (Figure 2b). The detail structure refinement parameters for both low-pressure and high-pressure phases were summarized in Table S1 (Supporting Information).

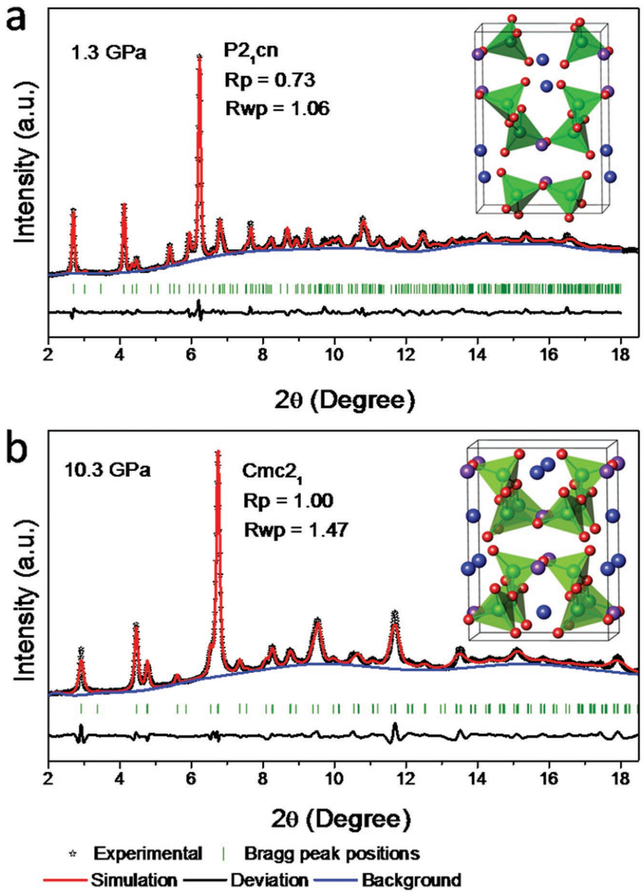

Figure 2. Typical Rietveld refinements of $KBiFe_2O_5$ in low- and high-pressure phases. a) Refinement of 1.3 GPa XRD data with space group $P2_1\,cn$, $a = 7.9416(1)$ Å, $b = 11.2614(3)$ Å, $c = 5.7108(4)$ Å, and $V = 532.12(3)$ Å^3. b) Refinement of 10.3 GPa XRD data with space group $Cmc2_1$, $a = 7.7683(3)$ Å, $b = 11.2614(4)$ Å, $c = 5.5187(2)$ Å, and $V = 482.78(6)$ Å^3. Insets in (a) and (b) are the corresponding refined low- and high-pressure structures of $KBiFe_2O_5$, respectively, while FeO_4 tetrahedra are highlighted in green and K, Bi, and O atoms in purple, blue and red respectively.

In general, the polarizations of the ferroelectric materials can be estimated from the crystal structures by the point charge model ($P_S = (\Sigma_i q(i)\delta d(i))/V$, where $q(i)$ is the nominal charge on the *i*th atom, $\delta d(i)$ is the displacement of the *i*th atom from its position in the pseudo centrosymmetric structure, and V is the unit cell volume).[33] To overcome the electrostatic repulsions, Fe and Bi in the distorted polyhedra displace away from the polyhedral centroids (shown as gray balls in **Figure 3**a) by 0.28 Å (d_{Fe}) and 0.84 Å (d_{Bi}), respectively. The displacement of Bi atoms is about three times larger than that of Fe atoms, which suggests that the BiO_6 octahedra are more distorted. However, due to the inconsistent orientations of the dipole moments of Fe, Bi, and K atoms (shown as arrows in Figure 3a), the components of the dipole moment vectors along the *a*- and *b*-axes are canceled and only maintained in opposite directions along the *c*-axis. Accordingly, the structural distortion in $KBiFe_2O_5$ results in spontaneous polarization (P_S) of ≈10.12 $\mu C\ cm^{-2}$ along the positive *c*-axis. This calculated polarization is much larger than the P_S of $KBiFe_2O_5$ (≈1.47 $\mu C\ cm^{-2}$)[28] at ambient pressure (Figure 3b) and comparable with that of $BaTiO_3$(≈26 $\mu C\ cm^{-2}$)[34] observed in bulk sample, which indicates that high pressure is a feasible route to produce a larger structural distortion that results in the enhanced ferroelectric properties. In order to confirm the above implication, the polarization-electric field hysteresis loops have been measured at room temperature under both 2.2 and 15.8 GPa with a two-point-probe sandwich-like connection mode (Figure S4, Supporting Information). As shown in Figure 3c,d, the well-saturated, single hysteresis loops, typical for the FE phase, were displayed for the sample under pressures. And also, two current peaks located in the vicinity of coercive field (E_c) are clearly observed in both phases, indicating the occurrence of ferroelectric switching. The observed saturation spontaneous polarizations (P_S), the remnant polarizations (P_r), and the coercive fields (E_c) were 2.79 $\mu C\ cm^{-2}$, 2.57 $\mu C\ cm^{-2}$, and 7.02 $kV\ cm^{-1}$ for 2.2 GPa; 12.23 $\mu C\ cm^{-2}$, 10.64 $\mu C\ cm^{-2}$, and 9.76 $kV\ cm^{-1}$ for 15.8 GPa. The remnant polarization P_r calculated for high pressure phase is about four times of the low-pressure phase, which definitely demonstrates the enhanced ferroelectric performance by high pressure.

The evolutions of lattice parameters of $KBiFe_2O_5$ under pressure are plotted in **Figure 4**a, indicating the anisotropic compressibility along different directions. The *b*-axis was found to be the most compressible direction, which gives the major contribution to the volume reduction. We noticed that there are many interspaces loosely arranged along the *c*-axis and the layered structure constructed by alternating blocks of $[Fe_2O_3]$ and $[(K,Bi)O_2]$ is perpendicular to the *b*-axis (Figure S5, Supporting Information). Commonly, the layered structure leads to spacious space and weak interaction between the layers,[35–37] so the structure dislocation and atomic displacement will more readily take place in it. Further compression

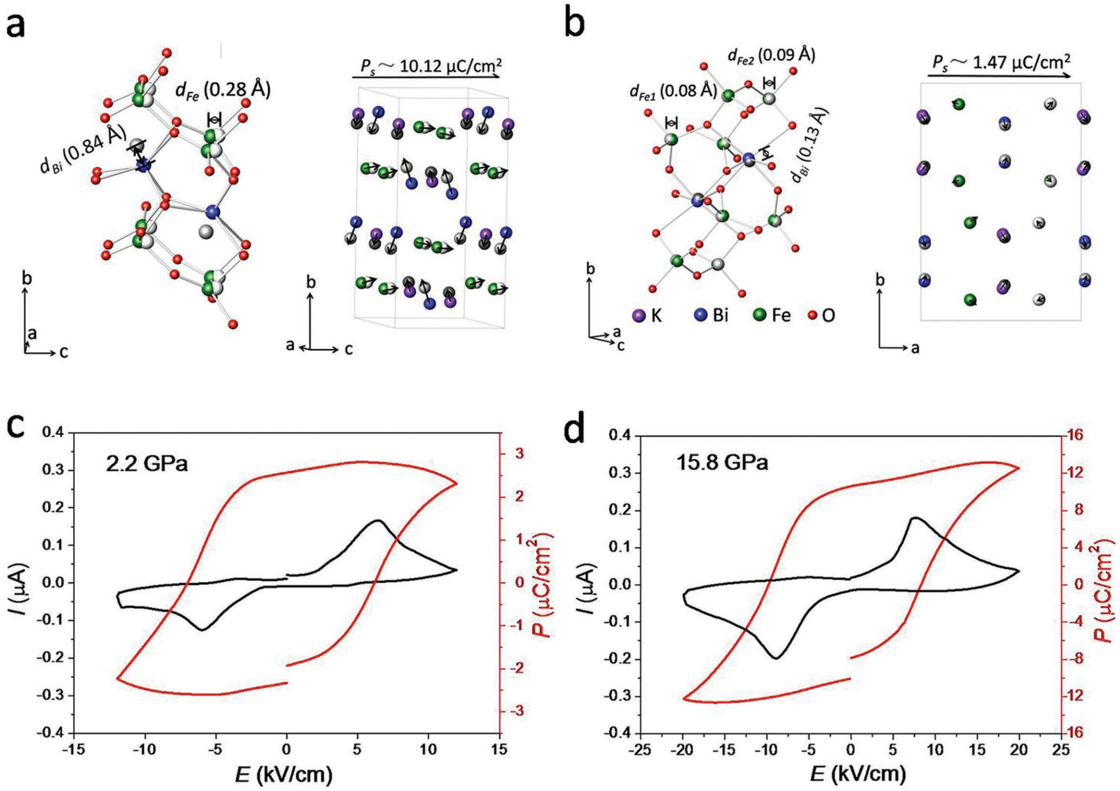

Figure 3. a) Crystal structure of the FeO_4/BiO_6 polyhedral framework under 10.3 GPa. The atomic displacements away from the FeO_4 and BiO_6 polyhedral site centroids (highlighted by gray balls, light gray balls for Fe, medium gray balls for Bi, and dark gray balls for K) are indicated as d_{Fe} (0.28 Å) and d_{Bi} (0.84 Å), respectively. Schematic ion locations and their associated dipole moments (the orientations of the dipole moments are shown as the arrows for each cation). The spontaneous polarization ($P_S \approx 10.12$ μC cm^{-2} along the positive *c*-axis) is obtained by summing dipole moments of cations in a unit cell assuming nominal charge for ions. b) Crystal structure of the FeO_4/BiO_6 polyhedral framework, schematic ion locations, and their associated dipole moments ($P_S \approx 1.47$ μC cm^{-2} along the positive *a*-axis) at ambient pressure. *I–E* and *P–E* hysteresis loops of a ferroelectric capacitor of Pt/$KBiFe_2O_5$ (5 μm thick)/Pt measured with applied voltages of 6 V/1 kHz for c) 2.2 GPa and 10 V/1 kHz for d) 15.8 GPa.

induced destabilization of the FeO_4 and BiO_6 polyhedral arrangement and consequently caused the phase transition to a denser phase at higher pressures. As shown in Figure 4b, the pressure dependent cell volume (V) could be well fitted to an isothermal Birch–Murnaghan equation of state (BM-EoS), where B_0 and B_0' are the bulk modulus and its pressure derivative, respectively[38,39]

$$p(V) = 1.5B_0\left[(V_0/V)^{7/3} - (V_0/V)^{5/3}\right] \times\left\{1+0.75(B_0'-4)\left[(V_0/V)^{2/3}-1\right]\right\} \quad (1)$$

The B_0 calculated from the fitting results for the LP and HP phases are, respectively, 63.4 ± 1.9 and 102.6 ± 3.8 GPa, which confirms that the HP phase is much denser and less compressible than the LP structure. Actually, the HP phase usually has a larger B_0 than the LP phase when pressure induces a structural phase transition.[40,41] For comparison, we also conducted the first-principles calculations on the unit cell volume versus pressure for both low and high pressure phases and obtained $B_0 = 53.1 \pm 1.2$ GPa, $V_0 = 561.6 \pm 1.1$ Å^3, $B_0' = 2.5$ for $P2_1\,cn$ phase, and $B_0 = 86.8 \pm 0.4$ GPa, $V_0 = 482.5 \pm 0.4$ Å^3, $B_0' = 4.2$ for $Cmc2_1$ phase. Although there are discrepancies of B_0 and V_0 with experimental data, i.e., ≈11%–16% and ≈3%–7%, respectively, the overall trend is consistent with the experimental observations. Based on the calculated *E–V* curves and their EOS parameters (Figure 4c), the static enthalpy differences (ΔH) were calculated and plotted in Figure 4d, and its zero position is corresponding to the initial volume of $KBiFe_2O_5$ at ambient pressure. A clear crossover of enthalpy lines at 11.6 GPa indicates a phase transition from $P2_1\,cn$ phase to $Cmc2_1$ phase, which is consistent with XRD and Raman results.

As we known, bandgap is one of the key properties for photovoltaic materials. Hydrostatic pressure has been playing an effective role on modifying the physical/chemical properties in material science, including the bandgap adjustment.[24,27] In situ PL experiments on $KBiFe_2O_5$ under hydrostatic pressure up to 29.9 GPa were performed using a DAC. In our experiments, the PL signal of single-crystal $KBiFe_2O_5$ was measured first at ambient pressure (**Figure 5**a). The PL peak was found at about 765 nm (equivalent to 1.62 eV), which is consistent with the reported E_0 (1.60 eV) of $KBiFe_2O_5$ at room temperature.[28] The PL curves for $KBiFe_2O_5$ upon compression show a gradual red shift up to 810 nm (equivalent to 1.53 eV) at 30 GPa, indicating a clear bandgap closing. Upon pressure releasing, the high-pressure phase can regain the red emission located at 765 nm due to the restoration of the ambient crystalline structure. Derived from the measured PL spectra, the bandgap E_g exhibits a strong nonlinear shift on compression (Figure 5b).

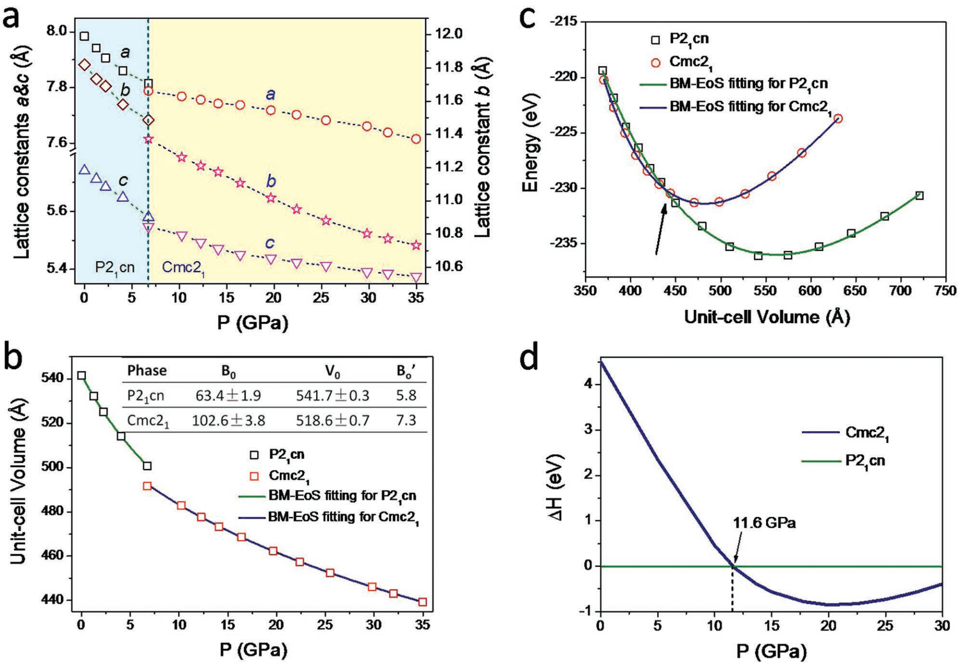

Phase	B_0	V_0	B_0'
$P2_1cn$	63.4±1.9	541.7±0.3	5.8
$Cmc2_1$	102.6±3.8	518.6±0.7	7.3

Figure 4. a) Evolutions of lattice parameters of $KBiFe_2O_5$ under compression. b) Unit-cell volume for $KBiFe_2O_5$. The solid lines show the fitting results obtained using the isothermal Birch–Murnaghan equation of state. c) Calculated total energy versus unit cell volume by spin-restricted calculations for different structures of $KBiFe_2O_5$ (energy–volume curves were fitted by the third BM-EoS). The arrow points to the critical pressure of the structural transition from orthorhombic $P2_1\,cn$ to $Cmc2_1$ phases. d) The enthalpy difference between $P2_1\,cn$ and $Cmc2_1$ structures as a function of pressure (the reference line is for $P2_1\,cn$ phase).

With increasing pressure, the bandgap decreased sharply from ambient pressure to 5 GPa followed by gentle decreasing to the highest pressure measured here, corresponding to the phase transition from LP to HP phase. To gain further insight into the electronic structure, first-principles calculations were carried out on the partial density of states. Based on the partial contributions of each element to the total density of state shown in Figure 5c, it is clear that the O 2p orbital and Fe 3d orbital contribute mostly to the valence band (VB) and conducting band (CB) of $KBiFe_2O_5$. Thus the pressure-induced bandgap narrowing can be mainly attributed to the shrinkage of FeO_4 tetrahedral layers rather than K or Bi cations (Figure S6, Supporting Information).

The resistivity of a semiconductor is a result of the coaction of the carrier concentration and the carrier mobility, which is one of the critical factors determining the photovoltaic performances of ferroelectrics.[8–11] To explore the pressure-induced transport property evolution of $KBiFe_2O_5$, in situ resistance measurements were carried out by using a four-point probe within DAC devices (shown as inset in **Figure 6**a). The Van de Pauw method[42] was utilized for the resistance determination derived from the equation $\exp(-\pi R_1/R_S) + \exp(-\pi R_2/R_S) = 1$, where R_1 and R_2 are the two resistances measured by the four-probe method and R_S is the sample resistance. Figure 6a shows the resistance evolutions of $KBiFe_2O_5$ as a function of pressure under compression and decompression. With increasing pressure, the resistance of the sample shows a rapidly decrease up to 5 GPa and then reach a gentle slope from 5 to 10 GPa, and finally become a flatland above 10 GPa. This trend is consistent with the evolution of the bandgap from PL spectra, which reveals the mutual dependency between the bandgap and the resistance. Actually, the resistance change should be correlated with the crystal and electronic structures tuned by pressure. The first sharp decreasing of resistance below 5 GPa is associated with the broadening of the valence and conduction bands, which caused by the shortening and bending of bonds.[43,44] Then the resistance begins to decrease gently at 5–10 GPa, which corresponds to increasing HP $Cmc2_1$ phase with consuming of LP $P2_1\,cn$ phase. Under further compression (>10 GPa), the slightly change of the resistance is associated with the pure HP phase deduced from XRD and Raman results. The minimum resistance reaches two orders of magnitude lower than the starting value. Based on rough estimation of the sample dimensions in DAC, the resistivity of HP phase at 30.5 GPa is close to $\approx 10^5\ \Omega$ cm, which is two orders of magnitude decreasing in resistivity from the reported ambient single crystal of $KBiFe_2O_5$ ($\approx 10^7\ \Omega$ cm),[28] five and one orders of magnitude decreasing comparing to the two other well-known ferroelectric PV materials with relative narrow bandgap, $BiFeO_3$ ($\approx 10^{10}\ \Omega$ cm)[32] and KBNNO ($\approx 10^6\ \Omega$ cm)[7] at ambient pressure, respectively. We also note that the pressure can markedly reduce the resistance of $BiFeO_3$ and even induce an insulator–metal transition above 45 GPa.[27] However, the reported HP phases (>3.6 GPa) of $BiFeO_3$ are all centrosymmetric[45] without ferroelectricity.

Considering the suitable bandgap and relative low resistivity, the pressure-induced polarized HP phase of $KBiFe_2O_5$ is presumably a promising ferroelectric PV material. In situ photoresponse of $KBiFe_2O_5$ under high pressure was also measured by using a two-point probe within DAC devices. From current–voltage

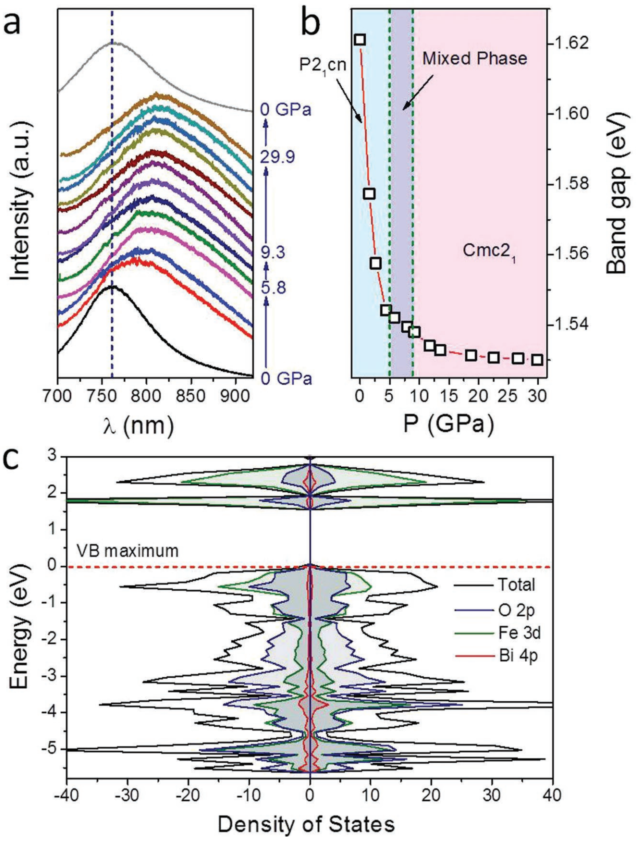

Figure 5. a) Room temperature PL spectra of $KBiFe_2O_5$ as a function of pressure during compression and decompression. A 633 nm and 17.3 mW laser was used for irradiation. b) Bandgaps derived from PL as a function of pressure. c) Calculated density of states from each element in the compound.

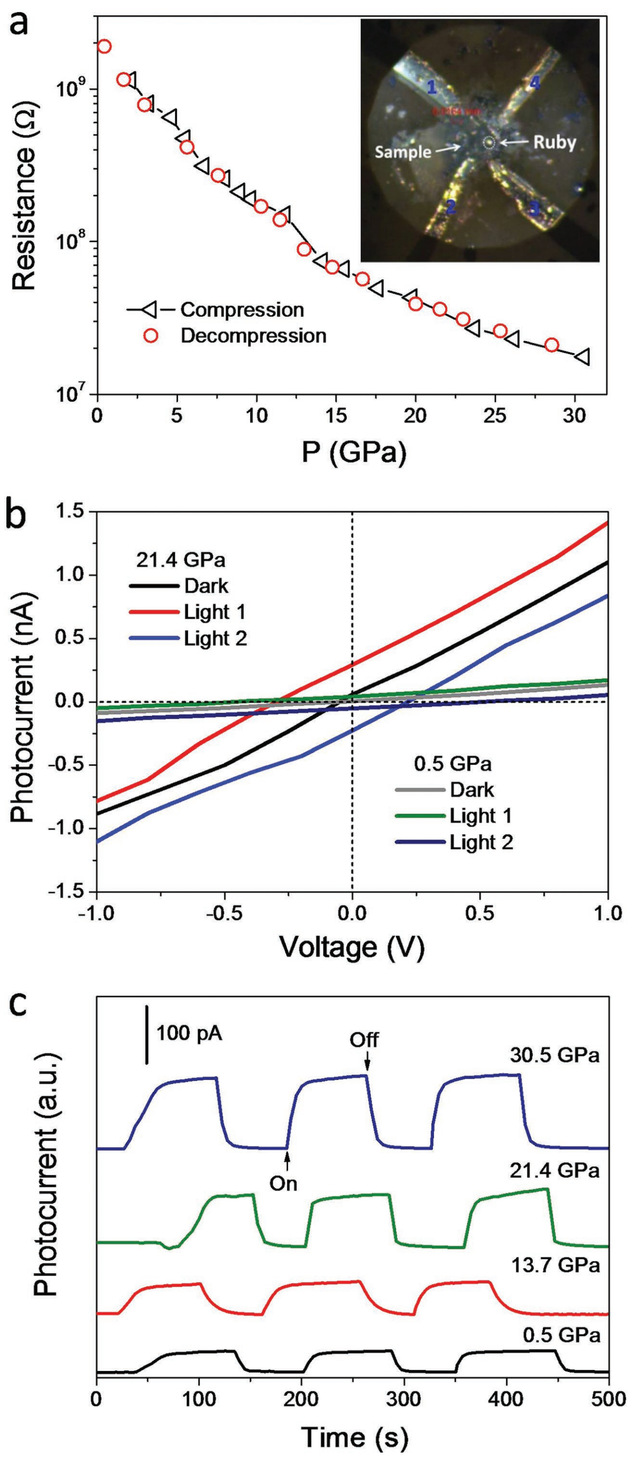

Figure 6. a) Electrical resistance of $KBiFe_2O_5$ during compression and decompression as a function of pressure (the inset displays microphotograph of the sample in DAC with Pt probes). b) Switchable bulk photovoltaic effect in $KBiFe_2O_5$ under 0.5 and 21.4 GPa. Black traces denote dark current; blue and red traces are photocurrent following poling under positive and negative voltages, respectively. c) Photocurrent of $KBiFe_2O_5$ during compression as a function of pressure.

(*I*–*V*) measurements, the remarkable photovoltaic behaviors can be observed under 0.5 and 21.4 GPa. Also, a reversal of photocurrent direction can be found by changing the poling direction (Figure 6b), which is indicative of the polar nature of the sample. The obtained open-circuit photovoltages V_{OC} and short-circuit photocurrents J_{sc} are about 0.31 V and 2.4 μA cm^{-2} at 21.4 GPa while 0.44 V and 0.72 μA cm^{-2} at 0.5 GPa. The obtained V_{OC} is much smaller than the one reported in single-crystal sample,[28] which is properly due to the polycrystalline sample without a regular arrangement of ferroelectric domains. As demonstrated previously,[5] larger photovoltages can be induced by periodically ordered domain walls in ferroelectrics. Actually, high V_{OC} are always observed in single-crystal samples or films with periodically ordered domain walls,[4,11,28,46] while the ferroelectric samples without such domain walls commonly generated small photovoltages lower than 1 V.[2,3,6–10] The EQE of the photovoltaic effect were also measured as 1.58×10^{-3} at 11.1 GPa and 4.95×10^{-4} at 1.3 GPa (Figure S7, Supporting Information), which is significantly larger than the value obtained for $BiFeO_3$ with the macroscopic measurements ($\approx 3 \times 10^{-7}$) but much lower than the value for the nanoscale measurement (≈1.0) due to the particular geometry of the top electrode.[11] Under entire selected pressures, two distinct states can be revealed in the on/off photocurrent plots, as shown in Figure 6c. It is worth noting that the photocurrent is growing continuously with increasing pressure and can reach up to about 160 pA (≈3.2 μA cm^{-2} for 5 mW cm^{-2} illumination) at 30.5 GPa, which is four times of that at 0.5 GPa. We also noticed that the response time for lights on/off switch is almost constant despite applied pressure. Although the photocurrent is still lower than the traditional PV materials, it is important for the emerging field of FE photovoltaics as a visible-light-absorbing material compared to some typical FE photovoltaics, such as $BiFeO_3$ (4 μA cm^{-2} for 10 mW cm^{-2} illumination[2]) and KBNNO (0.1 μA cm^{-2} for 4 mW cm^{-2} illumination.[7]) In addition, several efforts have been devoted to exploring the high-pressure effects on the photovoltaic materials such as Nb-doped TiO_2,[22] Ta_2O_5,[23] and $CH_3NH_3PbBr_3$,[26] few enhanced photoelectric performance has been reported so far. Considering this enhanced optoelectronic properties, the high-pressure phase of $KBiFe_2O_5$ is likely to be a great candidate for photosensitive switch applications.

In conclusion, pressure-induced structure transition and visible-light response have been studied in multiferroic oxide $KBiFe_2O_5$ as a function of hydrostatic pressures up to 35 GPa at room temperature. Synchrotron XRD, Raman spectroscopy, and first-principles calculation at high pressure revealed that the structure transition from low-pressure $P2_1cn$ to high-pressure $Cmc2_1$ phase is reversible and accompanied by significant volume reduction with hardening in bulk modulus, which is mainly associated with the shrinkage of FeO_4 tetrahedral layers. The bandgap shifts, electrical resistance, and photocurrent have been investigated by in situ high-pressure measurements, which show that hydrostatic pressure can greatly affect not only the crystal structure of $KBiFe_2O_5$ but also the photoelectric-related properties. In particular, the enhanced ferroelectric, electric transport, and photoelectric properties can be realized in the polarized HP phase, suggesting that the pressure-induced phase transition may offer a new route to explore new ferroelectric materials with improved photovoltaic performance.

Experimental Section

Sample Preparation and Characterizations: The detailed synthesis route of $KBiFe_2O_5$ has been described in previous work.[28] Briefly, 15 mL $Bi(NO_3)_3$ (0.2 M) and 30 mL $Fe(NO_3)_3$ (0.2 M) were initially mixed in a beaker by continuous stirring. And then, 50 g KOH was added to this solution. After cooling to room temperature, the mixture was transferred into a 100-mL Teflon-lined stainless steel autoclave with a filling capacity of 70%. Crystallization was carried out under autogenous pressure and 220 °C for 3 d. After the autoclave was cooled and depressurized, product was washed (with distilled water), sonicated, and harvested as dark brown crystals. The sample was confirmed as pure $P2_1cn$ phase with a lab X-ray diffractometer (a Rigaku D/Max-2000 diffractometer with Cu Kα radiation ($\lambda = 1.5418$ Å) at 40 kV, 100 mA, and a graphite monochromator at the secondary beam). The morphology and composition of the pristine sample were checked by SEM and EDS with a FEI Quanta 200F microscope operating at 20 kV.

In Situ High-Pressure Characterizations: A symmetrical DAC was employed to generate high pressure. A T-301 stainless steel gasket was pre-indented to 30 μm in thickness followed by laser-drilling the central part to form a 130 μm diameter hole to serve as the sample chamber. Precompressed $KBiFe_2O_5$ powder pallets and three small ruby balls were loaded into the chamber. In situ high-pressure angle-dispersive X-ray diffraction experiments were carried out at the 16 BM-D station of the High-Pressure Collaborative Access Team (HPCAT) at the Advanced Phonon Source (APS), Argonne National Laboratory. A focused monochromatic X-ray beam about 5 μm in diameter with a wavelength of 0.3099 Å was used for the diffraction experiments. Neon was used as the pressure-transmitting medium, and the pressures were determined by the ruby fluorescence method.[47] The diffraction data were recorded by a MAR345 image plate and 2D patterns were integrated to 1D patterns with the Fit2D program.[48] Rietveld refinements of the synchrotron XRD patterns were performed with the general structure analysis system code.[49] High-pressure Raman spectra were measured by a Raman spectrometer with a 633 nm excitation laser at HPSTAR. High-pressure PL spectra were recorded by the same spectrometer with a commercial 633 nm laser.

In Situ High-Pressure Ferroelectric, Resistance, and Photoelectric Measurements: *P–E* loops were measured at room temperature with varying the amplitude of the applied voltage at 1 kHz by a Zahner impedance analyzer. Electrical resistance measurements were conducted with a four-probe resistance test system in a diamond-anvil cell (see details in Figure S8, Supporting Information) at pressures up to 30.5 GPa. In order to achieve the electrical insulation between the electrical leads and metal gasket, a boron nitride layer was inserted between the steel gasket and diamond culet. Four platinum wires were arranged to contact the sample in the chamber for resistance measurements. A Keithley 6221 current source, 2182A nanovoltmeter, and 7001 switch system were used as the current supply, voltmeter, and voltage/current switcher, respectively. The resistance was determined by the Van de Pauw method.[42] Conductivity (*J–E*) measurements were performed by sweeping the voltage from the negative maximum to the positive maximum using a semiconductor characterization system (Keithley 4200). A 50 W incandescent lamp was used as the irradiation source (≈5 mW cm^{-2} on the sample). For zero-bias photocurrent measurements, the ceramic sample was first poled with a 10 V for 300 s, and its response was then measured in the dark and under illumination at selected pressure points.

First-Principles Calculations: The ab initio computations are based on density functional theory, with highly accurate projector augmented wave method as implemented in Vienna ab initio simulation package. The generalized gradient approximation (PBE-GGA)[50] methods were used in the study. The third- order Birch–Murnaghan finite strain equation of state (BM-EoS) was applied to fit our simulation results. The structure model for $KBiFe_2O_5$ at ambient condition ($P2_1cn$) was obtained from reported single-crystal structure. While the structure model for high-pressure polymorph ($Cmc2_1$) was from synchrotron XRD data. Antiferromagnetic structures were considered for both phases. Primitive unit cells were used for all calculations. The plane-wave cutoff was chosen as 400 eV according to previous calculations and the Brillouin zone was sampled on $4 \times 2 \times 6$ Monkhorst–Pack meshes[51] criterion for energy convergence was 1×10^{-6} Ryd. The effects of using a larger cutoff and number of *k* points on the calculated properties were tested and proved to be insignificant.

Supporting Information

Supporting Information is available from the Wiley Online Library or from the authors.

Acknowledgements

This work was financially supported by NSAF under Grant No. U1530402. W.Y. acknowledges financial support from the DOE-Basic Energy Sciences (BES) X-ray Scattering Core Program (DE-FG02-99ER45775). HPCAT operations are supported by DOE-NNSA under Award No. DE-NA0001974 and DOE-BES under Award No. DE-FG02-99ER45775, with partial instrumentation funding by NSF. APS is supported by DOE-BES, under Contract No. DE-AC02-06CH11357. G.Z. acknowledges financial support from NSF of China Grant No. 51402341.

Received: November 14, 2016

[1] Y. Yuan, T. J. Reece, P. Sharma, S. Poddar, S. Ducharme, A. Gruverman, Y. Yang, J. Huang, *Nat. Mater.* **2011**, *10*, 296.
[2] T. Choi, S. Lee, Y. J. Choi, V. Kiryukhin, S.-W. Cheong, *Science* **2009**, *324*, 63.
[3] R. Moubah, O. Rousseau, D. Colson, A. Artemenko, M. Maglione, M. Viret, *Adv. Funct. Mater.* **2012**, *22*, 4814.
[4] S. Y. Yang, J. Seidel, S. J. Byrnes, P. Shafer, C.-H. Yang, M. D. Rossell, P. Yu, Y.-H. Chu, J. F. Scott, J. W. Ager, L. W. Martin, R. Ramesh, *Nat. Nanotechnol.* **2010**, *5*, 143.
[5] J. Seidel, D. Fu, S. Yang, E. Alarcón-Lladó, J. Wu, R. Ramesh, J. W. Ager, *Phys. Rev. Lett.* **2011**, *107*, 126805.
[6] W. Ji, K. Yao, Y. C. Liang, *Adv. Mater.* **2010**, *22*, 1763.
[7] I. Grinberg, D. V. West, M. Torres, G. Gou, D. M. Stein, L. Wu, G. Chen, E. M. Gallo, A. R. Akbashev, P. K. Davies, J. E. Spanier, A. M. Rappe, *Nature* **2013**, *503*, 509.
[8] Y. Zang, D. Xie, X. Wu, Y. Chen, Y. Lin, M. Li, H. Tian, X. Li, Z. Li, H. Zhu, T. Ren, D. Plant, *Appl. Phys. Lett.* **2011**, *99*, 132904.
[9] X. Yang, X. Su, M. Shen, F. Zheng, Y. Xin, L. Zhang, M. Hua, Y. Chen, V. G. Harris, *Adv. Mater.* **2012**, *24*, 1202.
[10] D. Cao, C. Wang, F. Zheng, W. Dong, L. Fang, M. Shen, *Nano Lett.* **2012**, *12*, 2803.
[11] M. Alexe, D. Hesse, *Nat. Commun.* **2011**, *2*, 256.
[12] Y. Shi, Y. Guo, X. Wang, A. J. Princep, D. Khalyavin, P. Manuel, Y. Michiue, A. Sato, K. Tsuda, S. Yu, M. Arai, Y. Shirako, M. Akaogi, N. Wang, K. Yamaura, A. T. Boothroyd, *Nat. Mater.* **2013**, *12*, 1024.
[13] V. Keppens, *Nat. Mater.* **2013**, *12*, 952.
[14] Y. Inaguma, K. Tanaka, T. Tsuchiya, D. Mori, T. Katsumata, T. Ohba, K. Hiraki, T. Takahashi, H. Saitoh, *J. Am. Chem. Soc.* **2011**, *133*, 16920.
[15] R. Yu, H. Hojo, T. Mizoguchi, M. Azuma, *J. Appl. Phys.* **2015**, *118*, 094103.
[16] S. M. Young, A. M. Rappe, *Phys. Rev. Lett.* **2012**, *109*, 116601.
[17] S. M. Young, F. Zheng, A. M. Rappe, *Phys. Rev. Lett.* **2012**, *109*, 236601.
[18] A. Zerr, R. Riedel, T. Sekine, J. E. Lowther, W. Ching, I. Tanaka, *Adv. Mater.* **2006**, *18*, 2933.
[19] W. Yang, X. Huang, R. Harder, J. N. Clark, I. K. Robinson, H. K. Mao, *Nat. Commun.* **2013**, *4*, 1680.
[20] W. L. Mao, L. Wang, Y. Ding, W. Yang, W. Liu, D. Kim, W. Luo, R. Ahuja, Y. Meng, S. Sinogeikin, J. Shu, H.-K. Mao, *Proc. Natl. Acad. Sci. USA* **2010**, *107*, 9965.
[21] Y. Ma, M. Eremets, A. R. Oganov, Y. Xie, I. Trojan, S. Medvedev, A. O. Lyakhov, M. Valle, V. Prakapenka, *Nature* **2009**, *458*, 182.
[22] X. Lü, W. Yang, Z. Quan, T. Lin, L. Bai, L. Wang, F. Huang, Y. Zhao, *J. Am. Chem. Soc.* **2014**, *136*, 419.
[23] X. Lü, Q. Hu, W. Yang, L. Bai, H. Sheng, L. Wang, F. Huang, J. Wen, D. J. Miller, Y. Zhao, *J. Am. Chem. Soc.* **2013**, *135*, 13947.
[24] I. Zardo, S. Yazji, C. Marini, E. Uccelli, A. F. Morral, G. Abstreiter, P. Postorino, *ACS Nano* **2012**, *6*, 3284.
[25] I. P. Swainson, M. G. Tucker, D. J. Wilson, B. Winkler, V. Milman, *Chem. Mater.* **2007**, *19*, 2401.
[26] Y. Wang, X. Lü, W. Yang, T. Wen, L. Yang, X. Ren, L. Wang, Z. Lin, Y. Zhao, *J. Am. Chem. Soc.* **2015**, *137*, 11144.
[27] A. G. Gavriliuk, V. V. Struzhkin, I. S. Lyubutin, S. G. Ovchinnikov, M. Y. Hu, P. Chow, *Phys. Rev. B* **2008**, *77*, 155112.
[28] G. Zhang, H. Wu, G. Li, Q. Huang, C. Yang, F. Huang, F. Liao, J. Lin, *Sci. Rep.* **2013**, *3*, 1265.
[29] M. S. Leite, M. Abashin, H. J. Lezec, A. Gianfrancesco, A. A. Talin, N. B. Zhitenev, *ACS Nano* **2014**, *8*, 11883.
[30] G. Wang, S. Wang, Y. Cui, D. Pan, *Chem. Mater.* **2012**, *24*, 3993.
[31] W. Shockley, H. J. Queisser, *J. Appl. Phys.* **1961**, *32*, 510.
[32] D. Lebeugle, D. Colson, A. Forget, M. Viret, P. Bonville, J. F. Marucco, S. Fusil, *Phys. Rev. B* **2007**, *76*, 024116.
[33] R. Resta, D. Vanderbilt, *Theory of Polarization: A Modern Approach*, Vol. *105*, Springer, Berlin **2007**, p. 31.
[34] B. Jaffe, W. R. Cook, H. Jaffe, *Piezoelectric Ceramics*, Vol. *78*, Academic Press, London **1971**, p. 78.
[35] D. Li, R. B. Kaner, *Science* **2008**, *320*, 1170.
[36] Z. Ren, Z. Zhao, *Adv. Mater.* **2009**, *21*, 4584.
[37] J. M. Thomas, E. L. Evans, *Nature* **1967**, *214*, 167.
[38] F. Birch, *Phys. Rev.* **1947**, *71*, 809.
[39] F. D. Murnaghan, *Proc. Natl. Acad. Sci. USA* **1944**, *30*, 244.
[40] M. Nakayama, M. Nogami, M. Yoshida, T. Katsumata, Y. Inaguma, *Adv. Mater.* **2010**, *22*, 2579.
[41] G. Xiao, K. Wang, L. Zhu, X. Tan, Y. Qiao, K. Yang, Y. Ma, B. Liu, W. Zheng, B. Zou, *J. Phys. Chem. C* **2015**, *119*, 3843.
[42] L. J. van der Pauw, *Philips Res. Rep.* **1958**, *13*, 1.
[43] Y. Ma, M. Eremets, A. R. Oganov, Y. Xie, I. Trojan, S. Medvedev, A. O. Lyakhov, M. Valle, V. Prakapenka, *Nature* **2009**, *458*, 182.
[44] K. Arai, K. Kumata, K. Kadota, K. Yamamoto, H. Namikawa, S. Saito, *J. Non-Cryst. Solids* **1973**, *13*, 131.
[45] R. Haumont, P. Bouvier, A. Pashkin, K. Rabia, S. Frank, B. Dkhil, W. A. Crichton, C. A. Kuntscher, J. Kreisel, *Phys. Rev. B* **2009**, *79*, 184110.
[46] K. Yao, B. K. Gan, M. Chen, S. Shannigrahi, *Appl. Phys. Lett.* **2005**, *87*, 212906.
[47] H. K. Mao, J. Xu, P. M. Bell, *J. Geophys. Res.* **1986**, *91*, 4673.
[48] A. P. Hammersley, S. O. Svensson, M. Hanfland, A. N. Fitch, D. Häusermann, *High Pressure Res.* **1996**, *14*, 235.
[49] A. C. Larson, R. B. Von Dreele, *General Structure Analysis System (GSAS)*, Los Alamos National Laboratory Report, LAUR **2000**, 86.
[50] J. P. Perdew, K. Burke, M. Ernzerhof, *Phys. Rev. Lett.* **1996**, *77*, 3865.
[51] H. J. Monkhorst, J. D. Pack, *Phys. Rev. B* **1976**, *13*, 5188.